Title: Magnetic N-Enriched Fe3C/Graphitic carbon instead of Pt as an Electrocatalyst for the Oxygen Reduction Reaction

Authors: Hua Yang; xiaobai wang; peng zhang; wei wang; xiang lei

To be cited as: 10.1002/chem.201505138

Link to VoR: http://dx.doi.org/10.1002/chem.201505138

Magnetic N-Enriched Fe_3C/Graphitic carbon instead of Pt as an Electrocatalyst for the Oxygen Reduction Reaction

Xiaobai Wang[a], Peng Zhang[a], Wei Wang[a], Xiang Lei[a] and Hua Yang[a]*

Abstract: A series of $Fe_3C/C\text{-}N_x$ Nanoparticles (NPs) with different nitrogen content are prepared *via* a simple one-pot route. In the synthetic procedure, aniline and acetonitrile are simultaneously used as the carbon and nitrogen source. The effect of calcination temperature on the structural and functional properties of the materials is investigated. Magnetic measurement shows that the sample prepared at 800 °C ($Fe_3C/C\text{-}N_{800}$ NPs) possesses the highest M_s value of 77.2 emu/g. On testing as the oxygen reduction reaction (ORR) catalysts, the sample prepared at 750 °C ($Fe_3C/C\text{-}N_{750}$ NPs) shows the best ORR performance among the series, with a more positive onset potential (+0.99 V vs RHE), higher selectivity (number of electron transfer n ~ 3.93), longer durability, and stronger tolerance against methanol crossover than commercial Pt/C catalysts in a 0.1 M KOH solution. Moreover, in acidic solution, the the excellent ORR activity and stability is also exhibited.

Keywords: Fe_3C/C nanoparticles; sol-gel method; magnetic properties; fuel cells; oxygen reduction reaction

Introduction

Highly active and durable catalysts for the ORR are of great significance for large scale application of fuel cells.[1] The state-of-the-art catalysts are Pt-based materials,[2] however, they still suffer from several serious problems, including prohibitive cost,[3] limited availability, poor durability and the issue of methanol crossover;[4] these obstacles hamper the commercialization of this technology. Thus, the exploration of highly active non-platinum catalysts (NPMCs) for the four electrons ORR with comparable electrochemical performance is a paramount subject for fuel cells.[5]

Considering the harsh ORR conditions, it has been found that only a few types of materials are active and durable, such as carbon-accompanied transition metal-nitrogen composites (M-N-C, with M=Fe, Co, etc.)[6], metal-free N-doped carbon materials[7] and transition metal-carbon materials,[8] etc. Among the best is the M-N-C catalyst where the active sites are believed to involve surface nitrogen coordinated with metals.[5b]

Very recently, researchers reported a new type of NPMC based on Fe_3C which was active towards ORR. Hou et al. fabricated N doped Fe/Fe_3C@C nanoboxes supported on reduced graphene oxide sheets as ORR catalysts in alkaline media.[9] Yang et al. found that the N-doped bamboo-like carbon nanotube/Fe_3C nanoparticles (NPs) exhibited excellent ORR activities in both alkaline and acidic media.[10] Though interesting, limited information is known about the role of the Fe_3C phase in catalysis, probably owing to two main aspects: 1) the morphology of the catalysts is very important. As Hou and Yang's example,[9-10] only the regular shaped catalysts can exhibit excellent ORR activities. 2) it has been found that the prepared Fe_3C-based catalysts contain a certain amount of surface nitrogens, suggesting the possible presence of $Fe\text{-}N_x$ or/and $C\text{-}N_x$ moieties, and the $Fe\text{-}N_x$ and $C\text{-}N_x$ moieties are probably active towards ORR.[11] More exactly, the nitrogen-induced charge delocalization can facilitate the bridge model chemisorption of O_2 on the N-doped Fe_3C catalysts, which can effectively weaken the O–O bonding to promote the ORR.[12]

For the present view, the selectivity of oxygen reduction is quite important, that is the four electrons reaction or two electrons reaction. As Liu's example, non-N-doped carbon generated about 80% H_2O and 20% H_2O_2.[13] It should be pointed out that the formation of H_2O_2 is undesired, because it reduces the effective cathodic current, contaminates the surroundings of the catalyst, and corrodes the polymer membrane present in fuel cells. On the other hand, N-doped carbon generated more than 96% H_2O and less than 4% H_2O_2, which means that doping nitrogen on carbon not only favorable for the ORR activity, but also improves the selectivity towards oxygen reduction. Within this context, it is extremely important to maximize the nitrogen content in the ORR catalysts, so that make the catalysts exhibit the best ORR activity. However, most of current synthetic routes produce ORR catalysts are complicated and nitrogen content and morphology are uncontrollable, which are highly important and urgent problem need to be solved.

In this paper, we firstly report a simple one-pot route to synthesize Fe_3C NPs encased by uniform graphitic shells by directly calcinating the matrix of ferric chloride, aniline and acetonitrile under nitrogen atmosphere. By varying the calcination temperatures, a series of materials with different nitrogen contents (hereafter referred to as $Fe_3C/C\text{-}N_x$, x is the calcination temperature) are obtained. Magnetic measurements reveal that all of the as-synthesized $Fe_3C/C\text{-}N_x$ NPs display ferrimagnetic behavior at room temperature. On testing as the ORR catalysts, the $Fe_3C/C\text{-}N_x$ NPs exhibit excellent activities and stabilities in alkaline media.

[a]College of Chemistry, Jilin University，Changchun,130012 (P.R. China)
E-mail: huayang86@sina.com
Supporting information for this article is given via a link at the end of the document.

Results and Discussion

Structure and morphology

Fig. 1 (a) shows the XRD patterns of the four kinds of $Fe_3C/C\text{-}N_x$ (x= 650, 700, 750, 800 °C) NPs.

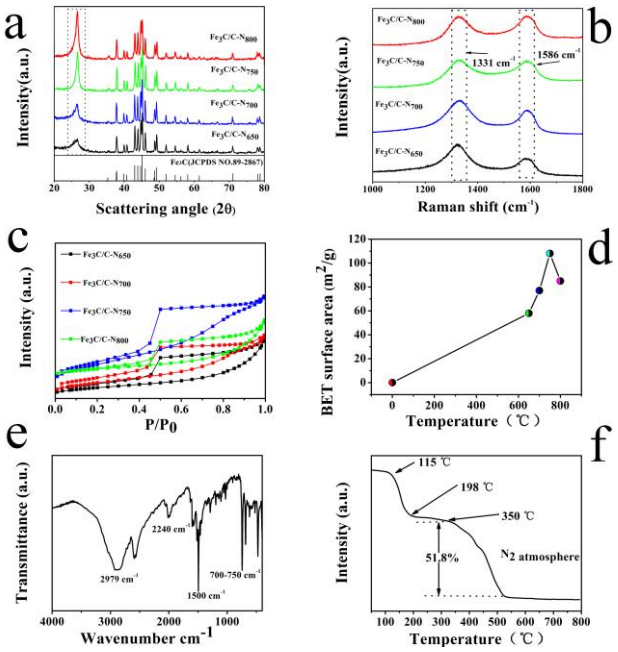

Figure 1 (a) XRD patterns, (b) Raman spectra, (c) N_2 sorption isotherm and (d) BET surface areas of the as-synthesized $Fe_3C/C\text{-}N_x$ (x= 650, 700, 750, 800 °C) NPs. (e) FT-IR spectrum, and (f) TGA curve of $Fe_3C/C\text{-}N_x$ – precursor.

One can see that all of the diffraction peaks are in good agreement with that of the Fe_3C (JCPDS card no. 89-2867). The nano-size nature of the $Fe_3C/C\text{-}N_x$ samples can be deduced from these strong and broaden peaks. A sharp peak appears at 2θ = 26.5° is ascribed to a crystalline structure of carbon (JCPDS card no. 26-1079). Note that with increasing the pyrolysis temperature from 650 to 800 °C, this peak is enhanced. This may be due to that the high temperature provides enough energy to promote the formation of crystalline carbon (here refer to graphitic carbon). Raman spectra are used to support this view. As can be seen in Figure 1 (b), the G-band for graphitic carbon appears at *ca.* 1586 cm^{-1} and the D-band for amorphous carbon[14] locates at *ca.* 1331 cm^{-1}. Typically, the relative intensity ratio of the D-band to the G-band (I_D/I_G) reveals the degree of graphitization of samples. The values for the four kinds of $Fe_3C/C\text{-}N_x$ NPs are 2.52, 1.97, 1.05 and 0.97, respectively. Among the series, $Fe_3C/C\text{-}N_{800}$ NPs has the lowest (I_D/I_G) value and so it has the highest degree of graphitization, confirming that the high temperature is the key factor in the formation of graphite carbon. This result is consistent with the XRD analysis. The point is that the degree of graphitization relates closely to the ORR performance and magnetic parameters of the materials.[10, 15]

Figure 1 (c) depicts the N_2 adsorption / desorption isotherm of the four kinds of $Fe_3C/C\text{-}N_x$ NPs. All samples exhibit type IV isotherms with hysteresis loops, signifying that the samples possess micro- and mesopores.[16] The unrestricted adsorption is confirmed by the hysteresis loop in the high pressure regime and the increase gas uptake at P/P_0 > 0.90 suggests that there are slit-like and bottle-like pores in the samples. BET yields the specific surface area for the four kinds of $Fe_3C/C\text{-}N_x$ NPs are 59, 77, 110 and 86 m^2/g respectively as shown in Fig 1 (d). One can see that with increasing the pyrolysis temperature, the specific surface area is increased. However, comparing with the $Fe_3C/C\text{-}N_{750}$ NPs, the specific surface area for $Fe_3C/C\text{-}N_{800}$ NPs is decreased, indicating that the high temperature likely leads to the collapse of the mesopores. In other words, the specific surface area reaches the maximum when the sample is prepared at 750 °C.

To investigate the formation mechanism of the $Fe_3C/C\text{-}N_x$ NPs, FTIR and TGA are performed to analysis the precursor of $Fe_3C/C\text{-}N_x$ NPs. Figure 1 (e) shows the FTIR spectrum of the precursor in the 400-4000 cm^{-1} region. The 1300-1500 cm^{-1} region is ascribed to the saturated C-H deformation vibration. The presence of the bands at 2240 cm^{-1} and 2979 cm^{-1} are the characteristic of the C-N and C-H stretching vibrations.[17] The existence of these bands confirms that there is acetonitrile in the precursor. Then the relative weakness of the band at 700-750 cm^{-1} is indexed to the vibration of mono-substituted benzene. In addition, the ring stretch of quinoid and benzenoid forms is observed at 1580 and 1500 cm^{-1}.[18] These observations confirm that the existence of aniline. Note that, there are no peaks for ferrite or other iron containing phase signifying that the iron should be existed in ionic condition. Finally, due to the oxidation of aniline, there may be nitrobenzene or quinoid etc. in the precursor.

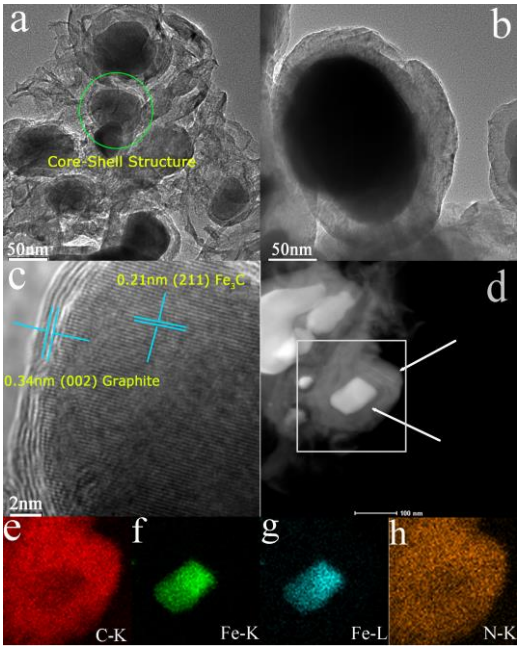

Figure 2(a) $Fe_3C/C\text{-}N_{750}$ NPs with core-shell structures and sheet-like carbon, (b) magnification image of a single particle, (c) HRTEM image of a particle, (d) HADDF-STEM image of $Fe_3C/C\text{-}N_{750}$ NPs and (e–h) the elemental mapping for the box region in (d).

Figure 1 (e) shows TGA curve for the precursor of $Fe_3C/C\text{-}N_x$ NPs which is measured in a N_2 atmosphere. There are four major steps of weight loss. The initial weight loss starts at below 198 °C is likely due to the vaporization of bound water. The second weight loss is very small, starting from 198 to 350 °C. This is the decomposition temperature range of nitrobenzene, quinoid and oligomers of aniline in a N_2 atmosphere. It seems a

reasonable deduction that part of these organics will be decomposed in this temperature range. The third weight loss of 51.8 % starts at 350 °C and ends at around 530 °C, which is most probably due to three important reasons: (1) The decomposition of organics[19]. (2) The nucleation of Fe_3C, and (3) The evaporation of $FeCl_3$.[20] Finally, the fourth weight loss is not very obvious at 1.8 % between 530 and 800 °C, which is likely due to the decomposition of some organic byproducts.

The morphology of $Fe_3C/C\text{-}N_{750}$ NPs is investigated by TEM and HRTEM. As shown in Figure 2 (a), the $Fe_3C/C\text{-}N_{750}$ NPs are embedded in a sheet-like carbon. There is a $Fe_3C/C\text{-}N_{750}$ particle with core-shell structure in the circle region. Figure 2 (b) represents an enlarged image of an isolated encapsulated particle. The image clearly indicates that the quasi-spherical particle has a core–shell structure with a complete and tight encapsulation. Figure 2 (c) shows a HRTEM image of a $Fe_3C/C\text{-}N_{750}$ particle. It is seen that the lattice fringes are 0.21 and 0.34 nm, which are attributed to an interplanar spacing of graphite (002) and Fe_3C (211) crystal plane, respectively. The high angle annular dark-field scanning TEM (HAADF-STEM, in Figure 2 (d)) reveals the positions of sheet-like carbon and the core-shell structure nature of $Fe_3C/C\text{-}N_{750}$ NPs. The elemental mapping results (Figure 2 (e-h)) demonstrate the uniform distribution of C, Fe and N. Importantly, N is detected over the whole area, which may be in favor of improving ORR performance of the materials.[21]

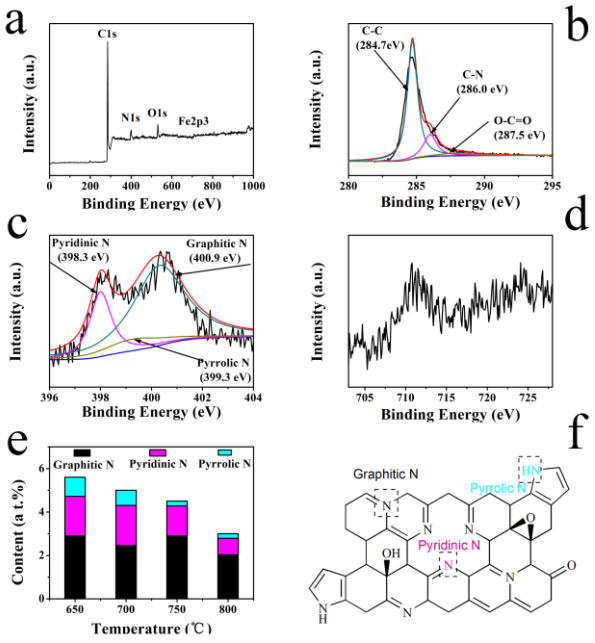

Figure 3 (a) Low-resolution XPS spectrum for $Fe_3C/C\text{-}N_{750}$ NPs, and high-resolution (b) C 1s, (c) N 1s and (d) Fe 2p XPS spectra for $Fe_3C/C\text{-}N_{750}$ NPs. (e) Concentrations of the three types of nitrogen in $Fe_3C/C\text{-}N_x$ samples obtained at different temperatures. (f) Illustration of three types of nitrogen in graphene.

Base on all of the above analysis, a possible mechanism for the formation of $Fe_3C/C\text{-}N_x$ NPs is proposed. First, when the aniline is added to the mixture of $FeCl_3$ and AN, part of it will be converted into nitrobenzene, quinoid or/and oligomers of aniline etc. immediately. Then the rest of aniline and AN will provide electrons to Fe^{3+} ions to form an iron-aniline-AN coordination structure. It is assumed that the [Fe (aniline) $_x$ (AN) $_{6-x}$] Cl_3 is the most possible one. During the water bath process, some AN may evaporate, leading to a stronger interaction between the Fe^{3+} ions and nitrogen atoms. By increasing the calcination temperature, quinoid or/and oligomers of aniline are decomposed to form a complicated carbon matrix. The [Fe (aniline) $_x$ (AN) $_{6-x}$] Cl_3 part is simultaneously transformed into Fe and nitrogen riched carbon matrix (Fe is surrounded by the nitrogen riched carbon matrix). When the temperature reaches the crystallization point of Fe_3C, the surrounding nitrogen riched carbon matrix will play the role of carbon source to react with Fe to form Fe_3C; In turn, the Fe_3C will play the role of catalyst to change the surrounding carbon matrix into graphite carbon. With the increase of pyrolysis temperature, the degree of graphitization of samples is increased. This has been demonstrated by the XRD and Raman analysis. In addition, there is a certain amount of surface nitrogen which has been demonstrated by the elemental mapping result, and it is most probably existed in the form of Fe-N_x or/and C-N_x moieties.

The Low-resolution XPS spectra for the as-synthesized $Fe_3C/C\text{-}N_x$ NPs are shown in Figure 3 (a) and Figure S1 (a). One can see that there are C 1s, N 1s, O 1s and Fe 2p in the spectra, confirming that the existence of these elements in the samples. The concentrations of the N and Fe in each sample are demonstrated in Table S1. It is shown that pyrolysis treatments at elevated temperatures (650-800 °C) lead to a significant decrease of Fe and N. Figure 3 (b) depicts the high-resolution C 1s spectrum of $Fe_3C/C\text{-}N_{750}$ NPs. It is deconvoluted into three peaks at 284.7, 286.0, and 287.5 eV, which are consistent with C-C, C-N, and O-C=O, respectively, signifying that a high degree of graphitization of this sample. In Figure 3 (c), the N 1s spectrum can be deconvoluted into three peaks at 398.3, 399.3 and 400.9 eV, which are assigned to pyridinic-N, pyrrolic-N and graphitic-N as illustrated in Figure 3 (f), signifying that nitrogen is indeed doped into the materials.[22] It should be note that pyridinic and pyrrolic-N can combine with Fe to form the Fe-N_x moieties, and researchers believe that the pyridinic-N and graphitic-N are benefit for ORR. Furthermore, according to the integrated peak areas, we quantify the concentrations of the three kinds of nitrogen which is shown in Table S1. It can be seen that graphitic-N is the dominated species in all samples (Figure 3 (e)), and $Fe_3C/C\text{-}N_{750}$ NPs possesses highest concentration of graphitic-N among the series which reaches to 2.9 at. %. It also can be seen that the concentration of pyridinic-N and pyrrolic-N are much lower in all samples. With increasing the calcination temperature, the concentration of pyridinic-N and pyrrolic-N are decreased markedly, indicating that the thermals stability of pyridinic-N and pyrrolic-N are weaker than graphitic-N. Further more, in Figure 3 (d), there is a negligible surface iron content on the $Fe_3C/C\text{-}N_{750}$ NPs from the high-resolution Fe 2p spectrum, which is likely due to the Fe_3C NPs are exclusively encased by the graphite carbon.

Magnetic properties

Magnetic measurements (Figure 4 (a)) reveal that all of the as-synthesized $Fe_3C/C\text{-}N_x$ NPs display ferromagnetism properties, and the $Fe_3C/C\text{-}N_{800}$ NPs has the highest M_s value of 77.2 emu/g compared to its high temperature annealed counterparts. The inset picture in Figure 4 (a) demonstrates that the materials can be easily recovered from suspensions. The M_s and H_c values *vs* calcinations temperature are summarized in Figure 4 (b). One can see that the M_s values tend to increase with increasing the calcinnation temperature, which is due to the

different crystallite sizes of the samples. In contrast, the coercivity (H_c) values are decreased from 175 Oe to 78.9 Oe. The detail magnetic data of the four $Fe_3C/C\text{-}N_x$ NPs are shown in Table. S2.

In this work, it is believed that the magnetic properties are relate closely to that of the electrochemical properties of the materials. As we all know, all of the magnetic nanomaterials possess the magnetocrystalline anisotropy, which are caused by two main reasons: 1) the combined effect of crystalline field and spin-orbit interaction 2) the effect of spin-orbit interaction to energy band. When the M_s value are increasing, the magnetocrystalline anisotropy will be decreased. The π electronics which are belong to the carbon shell tend to combine with the unoccupied orbital of the magnetic (Fe_3C) core easily, leading to the enhanced electrochemical properties of the magnetic materials.

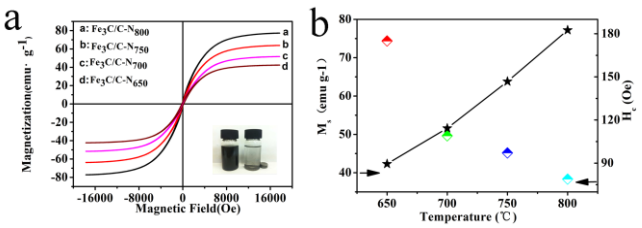

Figure 4 (a) *M-H* plots of the as-synthesized $Fe_3C/C\text{-}N_x$ NPs. (b) The graph of the M_s and H_c *vs* calcination temperature.

Electrochemical properties

Further, the as-synthesized $Fe_3C/C\text{-}N_x$ NPs are used as electrocatalysts for the ORR. The cyclic voltammetry (CV) and rotating ring-disk electrode (RRDE) techniques are used to analyze their electrocatalytic performance. Figure 5 depicts the CV curves of the as-synthesized $Fe_3C/C\text{-}N_x$ NPs which are obtained in a 0.1 M KOH solution saturated with N_2 or O_2 at the scan rate of 10 mV/s. One can see that there are quasi-rectangular voltammograms without redox peaks for all the four samples when the electrolyte is saturated with N_2. However, when the O_2 is involved, an obvious ORR peak is observed, signifying that these materials are sensitive toward ORR. Among the series, $Fe_3C/C\text{-}N_{750}$ shows the most positive peak potential of 0.82 V, suggesting that the highly pronounced ORR activity by $Fe_3C/C\text{-}N_{750}$ compared to its high temperature annealed counterparts. Note that, the $Fe_3C/C\text{-}N_{750}$ sample possesses the highest concentration of graphitic-N among the series (Figure 3 (e) and Table S1), signifying that graphitic-N likely play a dominant role in the determination of the ORR activity.

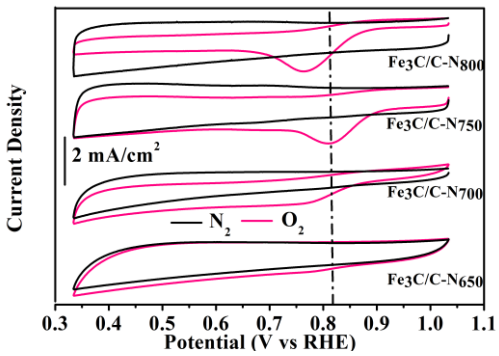

Figure 5 CV curves of $Fe_3C/C\text{-}N_{650}$, $Fe_3C/C\text{-}N_{700}$, $Fe_3C/C\text{-}N_{750}$, and $Fe_3C/C\text{-}N_{800}$ NPs in N_2-saturated, O_2-saturated 0.1 M KOH solution at a scan rate of 10 mV/s.

Figure 6 (a) shows the typical RRDE voltammograms of $Fe_3C/C\text{-}N_{750}$ and commercial Pt/C catalyst which are obtained at room temperature in O_2 - saturated 0.10 M KOH solution. It is seen that the $Fe_3C/C\text{-}N_{750}$ NPs shows a higher electrocatalytic activity towards ORR than commercial Pt/C catalyst, as indicated by its 30 mV more positive half-wave potential ($E_{1/2}$) compare to commercial Pt/C catalyst. Moreover, the onset potential is identified at +0.99 V for the $Fe_3C/C\text{-}N_{750}$ and +0.98 V for the commercial Pt/C, these are more positive than the Fe-C-N catalysts which are prepared by a complex methods in recent studies. From the RRDE test, it can also be calculated that the H_2O_2 percent yield (H_2O_2%) and the number of electron transfer (n) involved in ORR by using the following Equation 1 and 2:

$$H_2O_2\% = \frac{200 I_{Ring} / N}{I_{Ring} / N + I_{Disk}} \quad (1)$$

$$n = \frac{4 I_{Disk}}{I_{Ring} / N + I_{Disk}} \quad (2)$$

where N is the collection efficiency, I_{Disk} is the voltammetric currents at the risk electrode and I_{Ring} is the voltammetric currents at the ring electrode. In Figure 6 (b), it can be clearly seen that the yield of H_2O_2 for $Fe_3C/C\text{-}N_{750}$ is below 8.0 % at all potentials, corresponding to an average *n* of 3.93, close to that of the Pt/C catalyst. To evaluate the durability of $Fe_3C/C\text{-}N_{750}$ in alkaline solution for the ORR, linear sweeps between 0.4 and 1.04 V is applied.

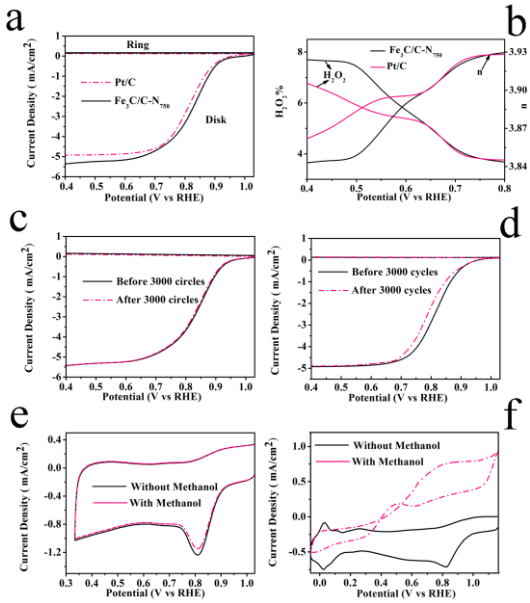

Figure 6 (a) RRDE voltammograms, (b) plots of H_2O_2 yield and number of electron transfer of $Fe_3C/C\text{-}N_{750}$ and Pt/C at the rotation rate of 1600 rpm. LSV curves of (c) $Fe_3C/C\text{-}N_{750}$ and (d) Pt/C for ORR before and after 3000 cycles. CV curves of (e) $Fe_3C/C\text{-}N_{750}$ and (f) Pt/C without and with 1.0 M CH_3OH. All of these experiments were carried out in O_2-saturated 0.10 M KOH solution.

In Figure 6 (c), it can be seen that there is a slight ORR polarization curve shift after 3000 cycles for $Fe_3C/C\text{-}N_{750}$ sample, while a significant ORR polarization curve shift is observed for commercial Pt/C catalyst as shown in Figure 6 (d). In addition, the resistance of the $Fe_3C/C\text{-}N_{750}$ sample and Pt/C catalyst toward methanol crossover is also investigated. As shown in Figure 6 (e), after the addition of 1 M methanol to 0.10 M KOH electrolyte solution, no significant change is observed in the ORR current for the $Fe_3C/C\text{-}N_{750}$ sample. In contrast, there is a significant change in the CV curve for the commercial Pt/C after methanol added. These results confirming that the $Fe_3C/C\text{-}N_{750}$ sample exhibits stronger tolerance against methanol crossover than commercial Pt/C catalysts.

Moreover, the $Fe_3C/C\text{-}N_{750}$ catalyst also exhibits excellent ORR activity and stability in acidic solution as shown in Figure S3. The onset potential is identified at +0.82 V for the $Fe_3C/C\text{-}N_{750}$, close to the +0.91 V for the commercial Pt/C catalyst. The H_2O_2% for $Fe_3C/C\text{-}N_{750}$ is below 5 %, corresponding to an average *n* of 3.84. The stability of $Fe_3C/C\text{-}N_{750}$ is better than Pt/C catalyst as shown in Figure S3 (c) and (d).

Based on the structure, morphology and composition of $Fe_3C/C\text{-}N_{750}$ NPs, we believe that three important aspects should be responsible for its excellent ORR activity and stability: (1) owing to the core-shell structure of the $Fe_3C/C\text{-}N_{750}$ NPs, there may be a host-guest electronic interaction between Fe_3C core and graphite carbon shell, making the outer surface of shell more active toward ORR[23]. (2) there may be a synergetic effect between sheet-like carbon and the encapsulated Fe_3C, which is relate closely to the ORR activity and stability of the $Fe_3C/C\text{-}N_{750}$ NPs.[24] (3) The high percentage of graphitic-N (2.9 at. %) in the $Fe_3C/C\text{-}N_{750}$ NPs can lead to the charge delocalization thus facilitate the bridge model chemisorption of O_2 on the $Fe_3C/C\text{-}N_{750}$ NPs, which can effectively weaken the O-O bonding to promote the ORR[25].

Conclusions

In summary, a series of $Fe_3C/C\text{-}N_x$ NPs with different nitrogen content were prepared by a simple one-pot route. In the synthetic procedure, aniline and AN are used as the carbon and nitrogen source. It is believed that an iron–aniline–AN coordination structure is involved in the nucleation process of Fe_3C. The effect of calcination temperature on the structural and functional properties of the materials is investigated. Magnetic measurements reveal that all of the as-prepared $Fe_3C/C\text{-}N_x$ NPs display ferrimagnetic behavior at room temperature, with the highest M_s value of 77.2 emu/g for $Fe_3C/C\text{-}N_{800}$ NPs. All of the as-prepared $Fe_3C/C\text{-}N_x$ NPs are also applied as the ORR catalysts. As a result, the $Fe_3C/C\text{-}N_{750}$ NPs emerges as a superior ORR electrocatalyst with highly pronounced electrocatalytic performance, long durability, high selectivity and strong tolerance against methanol crossover, these most likely due to the high percentage of graphitic-N and the unique structure of the $Fe_3C/C\text{-}N_{750}$ NPs. The findings of the synthetic route, the prepared materials of the unique structure, and the proposed mechanism paves a way to further development of active and durable ORR catalysts for fuel cell applications.

Experimental Section

Preparation of $Fe_3C/C\text{-}Nx$ NPs

The preparing process is depicted in Schematic 1. Firstly, 0.02 mol of $FeCl_3$ was added into 0.2 mol of acetonitrile (AN), stirring was needed. After 5 minutes, 0.3 mol of aniline was slowly added into above solution. The color of the solution gradually changed from yellow to dark brown. Subsequently, the mixture was transferred to a 80 °C water bath for 3 hours (h). During this process, the mixture became viscous. Finally, the viscous mixture was calcinated at controlled temperatures (650, 700, 750, or 800 °C) for 2 h in a N_2 atmosphere at the gas flow rate of 320 sccm.

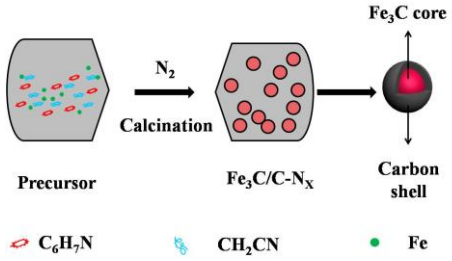

Schematic 1 Illustration of the preparation of the $Fe_3C/C\text{-}N_x$ NPs

Characterizations

The X-ray powder diffraction (XRD) patterns were recorded on a Shimadzu XRD-6100 using Cu Kα radiation (λ =0.15405 nm). Raman spectra were measured with a JobinYvon / HORIBA LabRam ARAMIS Raman spectrometer with the radiation from an air-cooled He Ne laser (633 nm). The Brunauer−Emmet−Teller (BET) surface area was determined by using a Micromeritics ASAP 2020 instrument at 77 K. The Fourier Transform Infrared (FTIR) Spectrometer spectrum was recorded on a Shimadzu IRAffinity-1 FTIR spectrometer using KBr pellets in the wavenumber range of 4000–400 cm^{-1}. Thermogravimetric analysis (TGA) was carried out using a Rheometric Scientific DSC QC (TA, USA) under a N_2 atmosphere at a heating rate of 5 °C/min. High resolution transmission electron microscopy (HRTEM) images were obtained with a Philips Tecnai G2 F20 High Resolution Transmission Electron Microscopy equipped with an EDS detector at an acceleration voltage of 100 kV. The magnetic properties were determined by using a LakeShore 7404 vibrating sample magnetometer (VSM) in the magnetic field of -17000 Oe - +17000Oe. Finally, the X-ray Photoelectron Spectroscopy (XPS) spectra were recorded using an ESCALAB 250 spectrometer with a mono X-ray source Al Kα excitation (1486.6 eV).

Electrochemical Measurement

Electrochemical measurements were performed in a standard three-electrode system controlled by a CHI 760D electrochemistry workstation (CH Instruments, Chenhua Co., China). A platinum wire was used as the counter electrode, an Ag/AgCl as the reference electrode and a catalyst-modified glassy carbon electrode (GCE) as the working electrode. The catalyst ink was prepared by adding 10 mg of catalyst into a mixture of deionized water, isopropyl alcohol, and Nafion (5.0 wt %) at a volume ratio of 20:1:0.075 to form a homogeneous suspension at the catalyst concentration of 2 mg/mL. The GCE was polished carefully to a mirror finish by using the 0.3 μm alumina slurries. After that, the GCE was sonicated in acetone, ethanol and deionized water successively to remove any bound particles, and dried under a gentle air stream. Then, a certain amount of the catalyst ink was evenly casted onto the pretreated GCE surface with a loading amount of 1.5 mg/cm^2. Finally, the modified electrodes were then dried under ambient conditions for electrochemical measurements. As a comparison, the commercial Pt/C catalyst was prepared according to the same procedure. Linear sweep voltammograms (LSV) were acquired in an O_2-saturated 0.1 M KOH solution and 0.1 M $HClO_4$ solution at a rotation rate of 1600 rpm. In the measurements, the Ag/AgCl reference electrode was calibrated with respect to a reversible hydrogen electrode (RHE).

Acknowledgements

This work was supported by the National Natural Science Foundation of China.

Keywords: nanoparticles •core-shell structures • magnetic properties • fuel cells • oxygen reduction reaction

References

[1] aM. K. Debe, *Nature* **2012**, *486*, 43-51; bB. C. Steele, A. Heinzel, *Nature* **2001**, *414*, 345-352.

[2] aY.-J. Wang, N. Zhao, B. Fang, H. Li, X. T. Bi, H. Wang, *Chemical reviews* **2015**, *115*, 3433-3467; bA. Chen, P. Holt-Hindle, *Chem. Rev* **2010**, *110*, 3767-3804; cS. E. Kleijn, S. Lai, M. Koper, P. R. Unwin, *Angewandte Chemie International Edition* **2014**, *53*, 3558-3586; dC. Wang, H. Daimon, Y. Lee, J. Kim, S. Sun, *Journal of the American Chemical Society* **2007**, *129*, 6974-6975; eS. Guo, S. Zhang, S. Sun, *Angewandte Chemie International Edition* **2013**, *52*, 8526-8544; fS. Sun, Z. Jusys, R. J. Behm, *Journal of Power Sources* **2013**, *231*, 122-133; gX. Zhou, Y. Gan, J. Du, D. Tian, R. Zhang, C. Yang, Z. Dai, *Journal of Power Sources* **2013**, *232*, 310-322.

[3] aX. Zhao, S. Chen, Z. Fang, J. Ding, W. Sang, Y. Wang, J. Zhao, Z. Peng, J. Zeng, *Journal of the American Chemical Society* **2015**, *137*, 2804-2807; bW. Wang, Y. Zhao, Y. Ding, *Nanoscale* **2015**, *7*, 11934-11939.

[4] W. Xia, J. Masa, M. Bron, W. Schuhmann, M. Muhler, *Electrochemistry Communications* **2011**, *13*, 593-596.

[5] aF. Jaouen, E. Proietti, M. Lefèvre, R. Chenitz, J.-P. Dodelet, G. Wu, H. T. Chung, C. M. Johnston, P. Zelenay, *Energy & Environmental Science* **2011**, *4*, 114-130; bZ. Chen, D. Higgins, A. Yu, L. Zhang, J. Zhang, *Energy & Environmental Science* **2011**, *4*, 3167-3192; cH. Yuan, Y. Hou, Z. Wen, X. Guo, J. Chen, Z. He, *ACS applied materials & interfaces* **2015**.

[6] aG. Wu, K. L. More, C. M. Johnston, P. Zelenay, *Science* **2011**, *332*, 443-447; bY. Hu, J. O. Jensen, W. Zhang, S. Martin, R. Chenitz, C. Pan, W. Xing, N. J. Bjerrum, Q. Li, *Journal of Materials Chemistry A* **2015**, *3*, 1752-1760; cJ. Wang, G. Wang, S. Miao, X. Jiang, J. Li, X. Bao, *Carbon* **2014**, *75*, 381-389; dS. Chao, Q. Cui, K. Wang, Z. Bai, L. Yang, J. Qiao, *Journal of Power Sources* **2015**, *288*, 128-135; eA. Muthukrishnan, Y. Nabae, C. W. Chang, T. Okajima, T. Ohsaka, *Catalysis Science & Technology* **2015**, *5*, 1764-1774.

[7] aN. Daems, X. Sheng, I. F. J. Vankelecom, P. P. Pescarmona, *Journal of Materials Chemistry A* **2014**, *2*, 4085-4110; bQ. Li, H. Pan, D. Higgins, R. Cao, G. Zhang, H. Lv, K. Wu, J. Cho, G. Wu, *Small* **2015**, *11*, 1443-1452; cW.-B. Luo, S.-L. Chou, J.-Z. Wang, Y.-C. Zhai, H.-K. Liu, *Small* **2015**, *11*, 2817-2824; dA. Zehtab Yazdi, K. Chizari, A. S. Jalilov, J. Tour, U. Sundararaj, *ACS Nano* **2015**, *9*, 5833-5845.

[8] aM. Kim, D.-H. Nam, H.-Y. Park, C. Kwon, K. Eom, S. Yoo, J. Jang, H.-J. Kim, E. Cho, H. Kwon, *Journal of Materials Chemistry A* **2015**, *3*, 14284-14290; bZ. Lu, G. Xu, C. He, T. Wang, L. Yang, Z. Yang, D. Ma, *Carbon* **2015**, *84*, 500-508; cM. Li, X. Bo, Y. Zhang, C. Han, A. Nsabimana, L. Guo, *Journal of Materials Chemistry A* **2014**, *2*, 11672-11682.

[9] Y. Hou, T. Huang, Z. Wen, S. Mao, S. Cui, J. Chen, *Advanced Energy Materials* **2014**, *4*.

[10] W. Yang, X. Liu, X. Yue, J. Jia, S. Guo, *Journal of the American Chemical Society* **2015**, *137*, 1436-1439.

[11] aY. Hu, J. O. Jensen, W. Zhang, L. N. Cleemann, W. Xing, N. J. Bjerrum, Q. Li, *Angewandte Chemie International Edition* **2014**, *53*, 3675-3679; bG. Zhong, H. Wang, H. Yu, F. Peng, *Journal of Power Sources* **2015**, *286*, 495-503.

[12] S. Gao, K. Geng, H. Liu, X. Wei, M. Zhang, P. Wang, J. Wang, *Energy & Environmental Science* **2015**, *8*, 221-229.

[13] aG. Liu, X. Li, J.-W. Lee, B. N. Popov, *Catalysis Science & Technology* **2011**, *1*, 207-217; bX. Zhou, Z. Yang, H. Nie, Z. Yao, L. Zhang, S. Huang, *Journal of Power Sources* **2011**, *196*, 9970-9974.

[14] F. Tuinstra, J. L. Koenig, *The Journal of Chemical Physics* **1970**, *53*, 1126-1130.

[15] X. Wang, P. Zhang, J. Gao, X. Chen, H. Yang, *Dyes and Pigments* **2015**, *112*, 305-310.

[16] X. Wang, P. Zhang, W. Wang, X. Lei, B. Zou, H. Yang, *RSC Advances* **2015**, *5*, 27857-27861.

[17] J. W. Chevalier, J. Y. Bergeron, L. H. Dao, *Macromolecules* **1992**, *25*, 3325-3331.

[18] M. I. Boyer, S. Quillard, E. Rebourt, G. Louarn, J. P. Buisson, A. Monkman, S. Lefrant, *The Journal of Physical Chemistry B* **1998**, *102*, 7382-7392.

[19] Z. Schnepp, S. C. Wimbush, M. Antonietti, C. Giordano, *Chemistry of Materials* **2010**, *22*, 5340-5344.

[20] W.-J. Liu, K. Tian, Y.-R. He, H. Jiang, H.-Q. Yu, *Environmental science & technology* **2014**, *48*, 13951-13959.

[21] W. Yang, X. Yue, X. Liu, J. Zhai, J. Jia, *Nanoscale* **2015**.

[22] P. Chen, L.-K. Wang, G. Wang, M.-R. Gao, J. Ge, W.-J. Yuan, Y.-H. Shen, A.-J. Xie, S.-H. Yu, *Energy & Environmental Science* **2014**, *7*, 4095-4103.

[23] aX. Zheng, J. Deng, N. Wang, D. Deng, W. H. Zhang, X. Bao, C. Li, *Angewandte Chemie International Edition* **2014**, *53*, 7023-7027; bH. T. Chung, J. H. Won, P. Zelenay, *Nature communications* **2013**, *4*, 1922.

[24] Y. Hu, J. O. Jensen, W. Zhang, Y. Huang, L. N. Cleemann, W. Xing, N. J. Bjerrum, Q. Li, *ChemSusChem* **2014**, *7*, 2099-2103.

[25] W. Niu, L. Li, X. Liu, N. Wang, J. Liu, W. Zhou, Z. Tang, S. Chen, *Journal of the American Chemical Society* **2015**, *137*, 5555-5562.

FULL PAPER

A series of $Fe_3C/C-N_x$ Nanoparticles (NPs) with different nitrogen content are prepared *via* a simple one-pot route. It can be seen that the materials exhibit excellent magnetic properties and ORR activities.

*Xiaobai Wang[a], Peng Zhang[a], Wei Wang[a], Xiang Lei[a] and Hua Yang[a]**

Page No. – Page No.

Magnetic N-Enriched Fe_3C/Graphitic carbon instead of Pt as an Electrocatalyst for the Oxygen Reduction Reaction

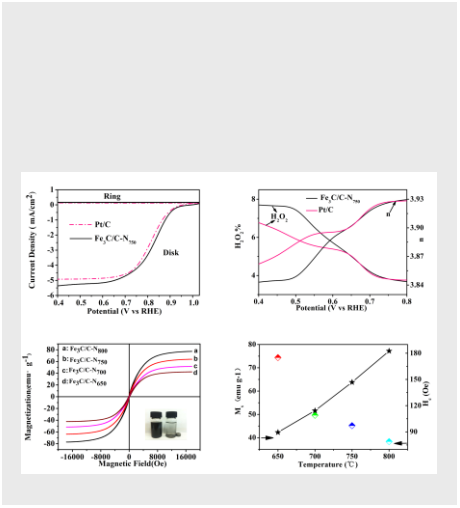

[a] Dr. X. Wang, P. Zhang, W. Wang, X. Lei, Prof. H. Yang

College of Chemistry, Jilin University
Changchun,130012 (P.R. China)

E-mail: huayang86@sina.com

Supporting information for this article is given via a link at the end of the document.